

Article

Assessment of the Thermo-Hydraulic Efficiency of an Indoor-Designed Jet Impingement Solar Thermal Collector Roughened with Single Discrete Arc-Shaped Ribs

Raj Kumar ¹, Erdem Cuce ^{2,*} , Sushil Kumar ^{3,*} , Sashank Thapa ¹ , Paras Gupta ¹, Bhaskar Goel ¹, C. Ahamed Saleel ⁴  and Saboor Shaik ^{5,*} 

- ¹ Faculty of Engineering and Technology, Shoolini University, Solan 173229, India; errajap@gmail.com (R.K.); mech12400@gmail.com (S.T.); kshgupta256@gmail.com (P.G.); goelbgoel@gmail.com (B.G.)
- ² Department of Mechanical Engineering, Faculty of Engineering and Architecture, Zihni Derin Campus, Recep Tayyip Erdogan University, Rize 53100, Turkey
- ³ Department of Physics, Hansraj College, University of Delhi, New Delhi 110007, India
- ⁴ Department of Mechanical Engineering, College of Engineering, King Khalid University, P.O. Box 394, Abha 61421, Saudi Arabia; ahamedsaleel@gmail.com
- ⁵ School of Mechanical Engineering, Vellore Institute of Technology, Vellore 632014, India
- * Correspondence: erdem.cuce@erdogan.edu.tr (E.C.); sushil8207@gmail.com (S.K.); saboor.nitk@gmail.com (S.S.)

Abstract: This study illustrates the impact of single discrete arc-shaped ribs (SDASR)-type artificial roughness on the performance of a jet impingement solar thermal collector (JISTC). The impact of parametric variations of SDASR on the Nusselt number (Nu_{sdr}), friction factor (f_{sdr}), and thermo-hydraulic performance (η_{sdr}) is examined. The spacer length (S_{sdr}) of the SDASR was changed from 0 mm to 300 mm in stages of 100 mm during the experiment. The fixed parameters of the SDASR were a relative discrete distance (D_d/L_o) of 0.67, relative discrete width (g_w/H_r) of 0.87, relative rib height (H_r/H) of 0.047, relative rib pitch (P_r/H) of 1.7, angle of an arc (α_{sdr}) of 60° , jet diameter ratio (D_j/D_{hy}) of 0.065, streamwise pitch ratio (X/D_{hy}) of 1.72, and spanwise pitch ratio (Y/D_{hy}) of 0.82. The Reynolds number (Re) was altered from 3000 to 19,000. The Nu_{sdr} and f_{sdr} of a JISTC with a roughened absorber plate was found to be enhanced by 5.25 and 5.98 times as compared to an STC without artificial roughness. The optimal findings of Nu_{sdr} , f_{sdr} , and η_{sdr} were achieved at $S_{sdr} = 0$ mm. The maximum value of the η_{sdr} obtained at $S_{sdr} = 0$ mm was 2.9.

Keywords: solar thermal collector; spacer length; friction factor; single discrete arc-shaped ribs; thermo-hydraulic performance



Citation: Kumar, R.; Cuce, E.; Kumar, S.; Thapa, S.; Gupta, P.; Goel, B.; Saleel, C.A.; Shaik, S. Assessment of the Thermo-Hydraulic Efficiency of an Indoor-Designed Jet Impingement Solar Thermal Collector Roughened with Single Discrete Arc-Shaped Ribs. *Sustainability* **2022**, *14*, 3527. <https://doi.org/10.3390/su14063527>

Academic Editor: Luca Cioccolanti

Received: 8 January 2022

Accepted: 8 March 2022

Published: 17 March 2022

Publisher's Note: MDPI stays neutral with regard to jurisdictional claims in published maps and institutional affiliations.



Copyright: © 2022 by the authors. Licensee MDPI, Basel, Switzerland. This article is an open access article distributed under the terms and conditions of the Creative Commons Attribution (CC BY) license (<https://creativecommons.org/licenses/by/4.0/>).

1. Introduction

The consumption of energy has been rising exponentially due to the revolution in manufacturing sectors, industrial sectors, and population growth worldwide. This need for energy is fulfilled by using petroleum, natural gas, coal, etc. Effective and efficient use of energy resources is the requirement of the present era. A flat STC is basically a heat exchanger which transfers the radiant energy of the incident sunlight to the sensible heat of a working fluid (liquid or air). It is used for space heating, solar crop drying, seasoning of timber, curing of industrial products, etc. The TP of an STC is generally poor because of low h_c among the absorber plate and the moving fluid (air) which rises the absorber plate temperature, leading to larger heat losses resulting in poor TP of such collectors. In order to enhance the TP of such collectors, heat has to be transferred efficiently.

Various heat transfer augmentation methods (HTAM) being used to raise HTR in heat exchangers have been described in studies [1–4]. Various techniques for the optimization of geometrical parameters have been proposed [5]. Out of various HTAM, an impinging jet raises HTR significantly. Turbulence promoters such as impinging jet and obstacles have

been used extensively to improve HTR. The impinging fluid jets (IMFJ) are used for different manufacturing functions, and a variety of jets are commonly used to attain a stable high HTR on the entire surface. Provision of blockage on the tested plate led to enhancement in the performance of solar air heater (SAH). The controlled IMFJ has been used in many fields, such as paper, gas turbine, textile, food, and low and high temperature surfaces. Various factors influence the HTR in the methods of multiple jet impingements. The solar receivers operate under the equivalent principle, dissipating solar energy and effectively transmitting heat energy to the fluid [6–8]. The IMFJ effectively employed partial air gaps and caused higher HTR. Primarily through the highest flow speed, the HTR provided by the IMFJ is three times greater than those produced by traditional convection cooling equipment. IMFJ is utilized in industrial fields such as plane ventilation, paper materials, etc. Many studies on the HT and friction factor characteristics have been performed [9–11].

Aboghrara et al. [12] designed an SAH to explore the influence of jet impingement on the corrugated heated plate by altering the mass flow rate of the air. They observed that the thermal efficiency of the heated plate rises with a rise in mass flow rates of air because of the disturbing of the laminar sub-layer that produces elevated turbulence of air, which results in more heat transfer. Thermal efficiency of the designed SAH was found to be fourteen percent more as compared to the smooth heated plate. Roy et al. [13] examined the Nu_{rs} and f_{rs} of a jet impingement SAH with an inclined surface. The Reynolds number was varied from 500 to 20,000 to analyze the Nu_{rs} and f_{rs} of SAH. Chauhan et al. [14] studied the thermo-hydraulic performances of JISTC. During the investigation, the Re , X/D_{hy} , Y/D_{hy} , and D_j/D_{hy} were varied. The results showed that the maximum efficiency of 70% was attained for a JISTC compared with a smooth STC. Babic et al. [15] developed a new cooling approach with a grinding cooling method. The grinding method mostly depends on water and air. In this process, a small amount of water is injected into the air jet, which further hits the grinding wheel and provides the cooling, whose results are better than those of the conventional coolants. A high-speed mist jet is a more effective and inexpensive way to clean the wheel and lessen the specific energies. Roger et al. [16] numerically examined the system with multiple air jets cooling for solar thermal applications. The multiple air jets impinge on the concave window surface of transparent window glass to acquire cooling. Symmetric arrangement with six and nine nozzles uniformly dispersed on the window circumference was evaluated. The findings show that the multiple air-cooling jet system with periodically modulated airflow has superior performance. Caliskan et al. [17] studied the HT characteristic of the circular jet impingement on the surface with V-SR and CD-SR ribs. Five surfaces with distinct rib height were investigated, and their influence on the HT along the wall was explored. The findings of impinging jet with ribs roughness were compared with the findings of conventional SAH. The outcomes indicated that the maximum HTR increase of 4.26% was attained with the V-SR arrangement. Chang et al. [18] explored the impact of rib roughness parameters with a circular jet on a heat transfer rate. The Reynolds number varied from 7000–15,000. The influence of the parameters on the HTR was further used to evaluate the efficiency of rib roughness within the 2D array of the circular jet. Yan et al. [19] analyzed the HT characteristics of the rib-roughened surface by using impinging elliptical jets. The experiment was conducted to explore the impact of angled ribs. The results show that with 45° V-ribs, a maximum heat transfer was obtained as compared with other angles of the ribs. Xing et al. [20] studied the impact of jet impingement with micro-rib roughness on the HT characteristics. The parameters considered during the investigation were cross-flow schemes, jet-to-plate spacing, and Re . The jet-to-plate distance of 3 resulted in the highest HT coefficients for the flat as well as the micro-rib-roughened plate. Goodro et al. [21] explored the impact of the hole distance on the h_c . In this experiment, the range of Re was from 8200 to 32,500, whereas the range of the Mach number was from 0.1 to 0.6. Spacing of the holes was either 8D or 12D, made by impinging jets. The results showed that the Mach number significantly affects the heat transfer coefficient. The findings suggested that the HT for both 8D and 12D spacing of holes increases with the increase in the Mach number. Huber et al. [22] experimentally

compared the HT to the perimeter and center jet confined using an impinging array of air jets. Contour plots were used to observe the difference between local Nu_{rs} distribution for perimeter and center jets. The results indicated that the contour for a constant Nusselt number for the perimeter jets had an oval shape. There was only a very small difference (15%) between the perimeter and center jet contours. Chambers et al. [23] proposed a computational and experimental study to enhance the cooling performance in the high cross-flow channel by designing elliptical and circular impingement holes. These holes increased the infiltration of the impinging jet inside the coolant channel. The findings suggested that the Nu_{rs} rose by 16% in the coolant passage (halfway downstream). For the first four holes, the Nu_{rs} increased by 28 to 77% under the condition that no extra cross-stream was present in the passage. Lewis et al. [24] optimized the rough surfaces' thermohydraulic performances with new efficiency parameters. The roughness function, which is the function of momentum transfer and heat transfer, is the most important parameter that influences the TP of the rough surfaces. Matheswaran et al. [25] experimentally examined the exergy efficiency of an STC with a single-pass double duct jet. The experiment was conducted for different ranges of geometrical parameters, such as $X/D_{hy} = 0.435-1.739$, $Y/D_{hy} = 0.435-0.869$, and $D_j/D_{hy} = 0.043-0.109$ and for $m_{sdr} = 0.002-0.023$ Kg/s. The results show that the exergy and energy efficiency of single-pass double duct jet SAH was enhanced by 22.4 and 21.2%, respectively, compared to SAH. Yadav et al. [26] used CFD analysis to compare the HT performances of a simple and impinging jet SAH. ANSYS fluent 14 software was employed to analyze the TP of JISAH and compared with a traditional air heater without jet impingement under similar circumstances. Both experiments were conducted under Reynold's number variations from 3800–16,000. The results show that HT in a jet impingement STC was 2.16 times higher than conventional SAH. Aboghrara et al. [27] conducted a study to explore the thermal performances of a jet impingement SAH with a corrugated plate. They compared the thermal performances of the proposed SAH with those of a conventional SAH. The results show that the proposed SAH's thermal performances were far superior to those of the conventional SAH. Rajaseenivasan et al. [28] analyzed the impact of the attack angle of jet impingement and the diameter of the nozzle on the heat transfer characteristic of the SAH. The attack angle and nozzle diameter were altered from 0° to 90° and 3 mm to 7 mm, respectively, during the experiment. The mass flow rate of the air was altered from 0.012 to 0.016 kg/s. The outcomes showed that the maximum performance was attained with an attack angle of 30° and a nozzle diameter of 5 mm. The highest thermal augmentation factor of 2.19 and efficiency of 55.8% were obtained with a mass flow rate of 0.016 kg/s. Goel et al. [29] experimentally explored the impact of X/D_{hy} , fin spacing ratio, and D_j/D_{hy} on the thermal performances of jet impingement SAH integrated with the array of fins. The experiment was performed for Re from 5700 to 11,700 and for m_{sdr} from 0.056 to 0.112. The results show that heat transfer was enhanced by 2.5 times for a JISTC with fins compared to conventional SAH. Similar works are also in the literature [30–34] which refer to the solar device operated using nanofluids with their mathematical models, jet impingements, numerical analysis, etc. [35–37]. D. García and J.I. Prieto [38] presented a heat exchanger for use in a solar engine micro co-generation unit. The different selection criteria were followed in designing the engine. The authors described the geometrical characteristics of the heater. They discussed the variables that can affect the pressure drop and HT characteristics. They also developed the correlations for the f_r and Stanton number under steady stream conditions. In all these studies, the previous works of distinct researchers reported that impinging jets enhance transfer rate and improve the performance of the SAH. However, no previous work has investigated the impact of spacer length variation on the η_{sdr} of a JISTC with single discrete arc-shaped ribs. Therefore, this work intends to investigate Nu_{sdr} , f_{sdr} , and η_{sdr} in a JISTC with single discrete arc-shaped ribs at distinct values of spacer lengths. The impinging jet STC diagram is depicted in Figure 1a. Jet impingement provides triple heat transfer coefficients due to thin impingement boundary layers, as presented in Figure 1b.

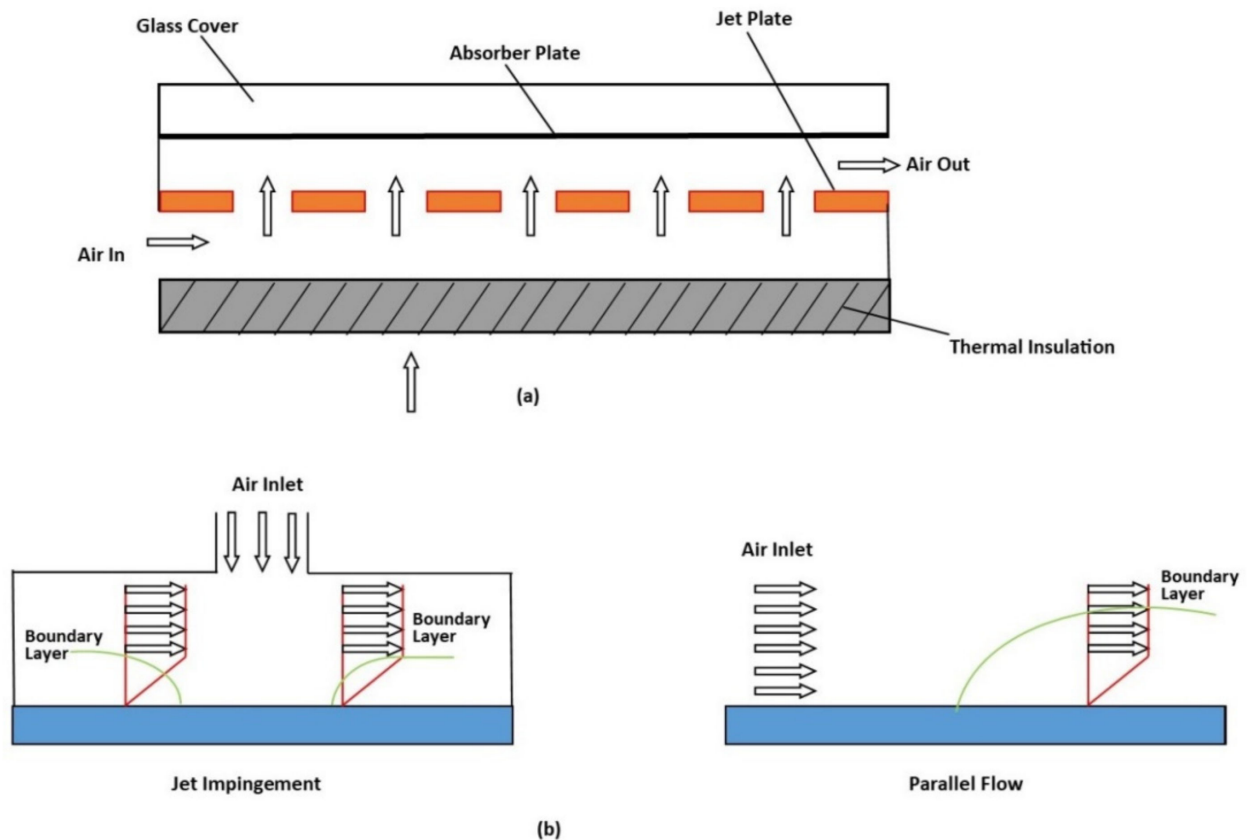


Figure 1. (a) Impingement jet solar thermal collector. (b) Comparison among boundary layers of jet impingement and parallel flow.

2. Roughness and Experimental Parameters

The aluminum wires were fixed on the galvanized iron plate (absorber plate) to create roughness. A standard-sized wooden cylinder was used to fabricate the desired shapes of wire on the absorber plate. The diameter of the cylinder used to construct the discrete arc-shaped ribs was determined using the following formula [38]:

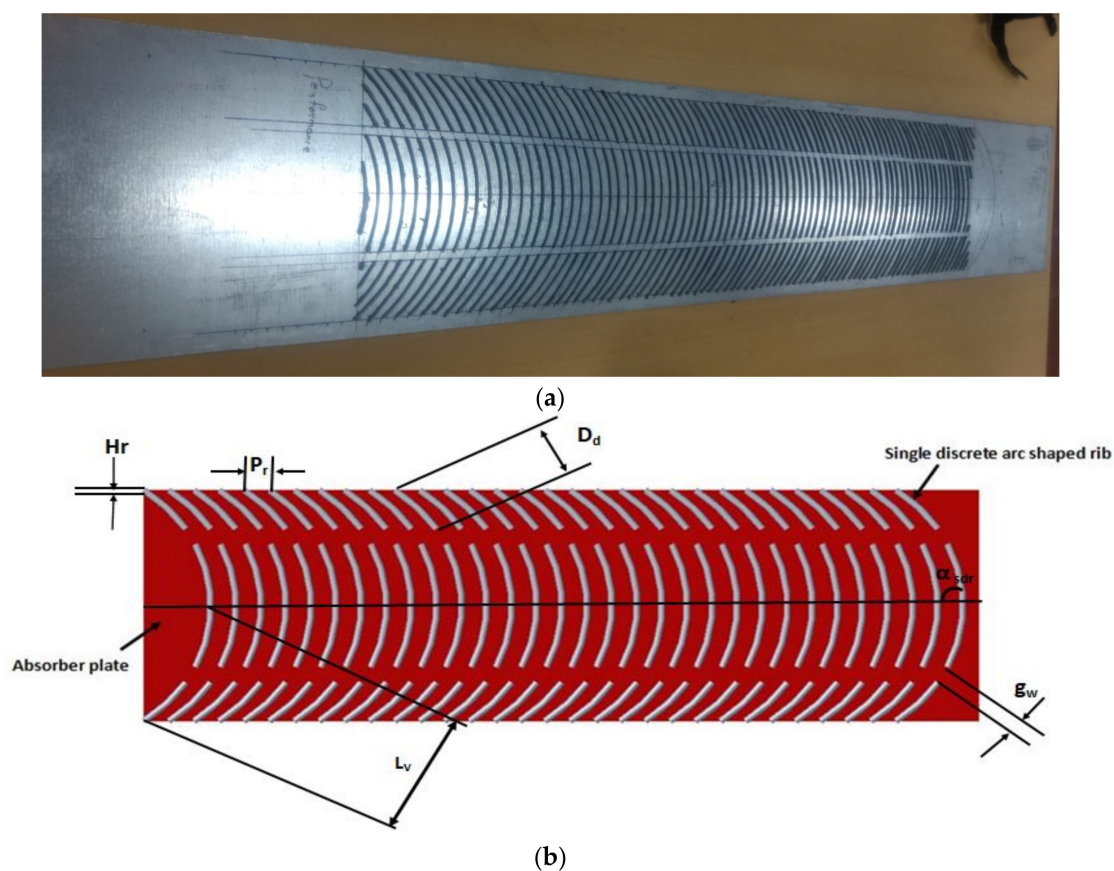
$$D_c = C_L / \cos(90 - \alpha) \quad (1)$$

where C_L is the chord length and α is angle of the arc.

The channel size was specifically chosen based in previous studies where the length of the channel (L_p) was 1200 mm, channel width (W) was 300 mm, and channel height (H) was 25 mm. The single discrete arc-shaped rib geometry has fixed values of D_d/L_v , g_w/H_r , H_r/H , P_r/H , α_{sdr} , X_s/D_{hy} , Y_s/D_{hy} , and varying values of S_{sdr} , respectively. An array of different geometric factors selected to conduct the experiments are depicted in Table 1. Figure 2a shows the pictorial view of single discrete arc-shaped ribs mounted on the absorber plate. Figure 2b illustrates the schematic view of single discrete arc-shaped ribs with parameters.

Table 1. An array of flow and geometric factors.

Geometric Factors			
Sr. No.	Factors	Symbols	Range
1.	Relative discrete distance	D_d/L_v	0.67
2.	Relative discrete width	g_w/H_r	0.87
3.	Relative rib height	H_r/H	0.047
4.	Relative rib pitch	P_r/H	1.7
5.	Angle of attack	α_{sdr}	60°
6.	Streamwise pitch ratio	X/D_{hy}	1.72
7.	Spanwise pitch ratio	Y/D_{hy}	0.82
8.	Jet diameter ratio	D_j/D_{hy}	0.065
9.	Spacer length	S_{sdr}	0 mm to 300 mm
10.	Absorber plate surface area	A_p	$36 \times 10^4 \text{ mm}^2$
11.	Orifice meter area	A_0	$10.17 \times 10^2 \text{ mm}^2$
12.	Height of duct	H	25 mm
13.	Width of duct	W	300 mm
14.	Length of test section	L_p	1200 mm
Flow Factors			
Sr. No.	Factors	Symbols	Range
1.	Reynolds number	Re	3000–19,000 (8 steps)
2.	Mass flow rate	m_{sdr}	0.008–0.05 kg/s (8 steps)
3.	Velocity	V_a	1.02–6.47 m/s (8 steps)

**Figure 2.** (a) Pictorial view of discrete arc-shaped ribs mounted on the absorber plate. (b) Schematic view of the single discrete arc-shaped ribs absorber plate.

3. Experimental Setup Details

The experimentation structure was fabricated and assembled as per the ASHRAE standard to examine the impact of single discrete arc-shaped ribs on the performance of JISTC. Significant parts of the test setup involve a wooden rectangular channel, a voltmeter, an ammeter, an orifice plate, an electric heater, a U-tube manometer, a high-pressure blower for propelling air, an inverter, control valves, a micro-manometer, thermocouples, a variable transformer, etc. Figure 3a presents a schematic diagram of a test arrangement with the impinging jet plate. Twenty-nine constantan-based thermocouples were used to measure the temperature at distinct places, as indicated in Figure 3b. The jet plate was made up of good quality plyboard with a sunmica sheet pasted on both sides to ensure a good smooth surface. Figure 3c illustrates the actual picture of the jet plate.

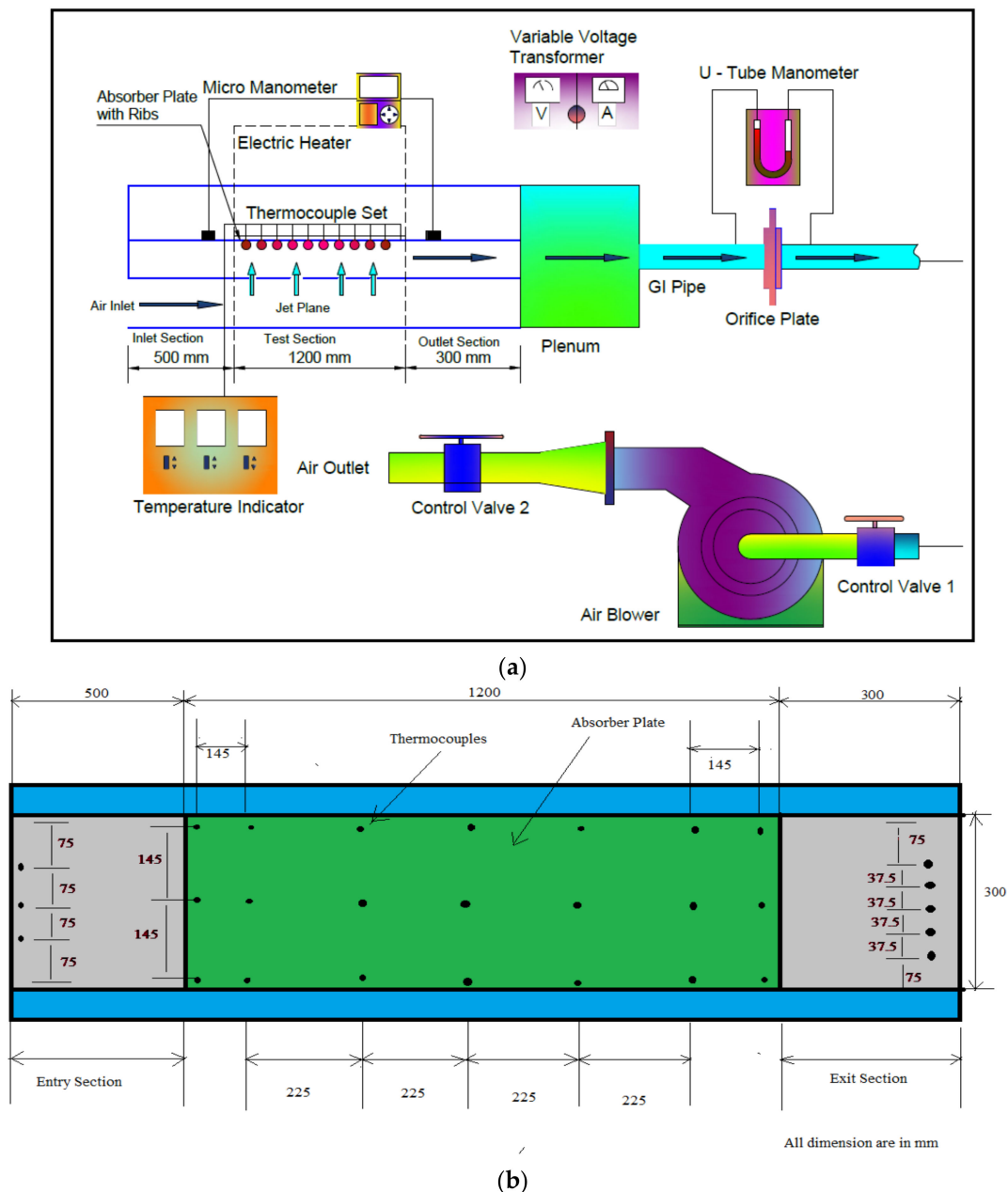


Figure 3. Cont.

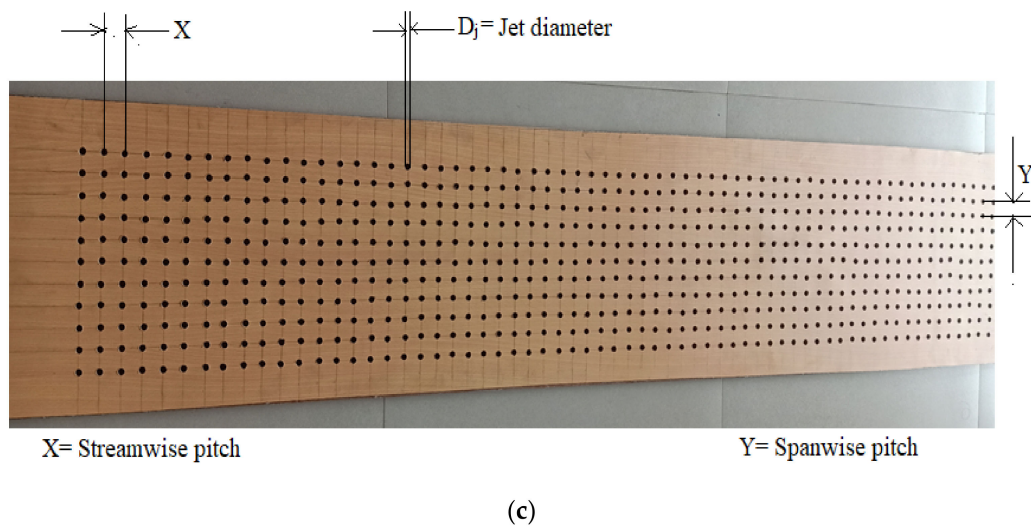


Figure 3. (a) Schematic view of JISTC. (b) Schematic view of thermocouple position on absorber plate. (c) Photographic view of jet plate.

A well-armed nichrome wire electric heater was used to transfer 1000 W/m^2 heat flux above an array of test portions. A variac and ammeter were employed to control and retain uniform heat flux throughout the experiment. Because of atmospheric effects, the peak solar insolation incident on a terrestrial surface normally oriented to the sun at noon on a clear day was on the order of 1 kW/m^2 . Therefore, a uniform heat flux of 1000 W/m^2 was used during the experiment. The electric heater was fabricated by combining loops of nichrome wire in series and parallel combinations located on the top wall of the test section. A sheet of mica was placed over the heater to ensure uniform radiations over the surface. The back side of the heater was insulated with glass wool to reduce the heat losses. A U-tube manometer was employed to record $(\Delta p)_0$. Moreover, suitable insulation was provided to reduce heat losses.

In the current experimental set up, a high-pressure blower for propelling air was used. Due to the small cross-section of the outlet of the blower, the flow was not fully developed inside the duct of the STC. To overcome this problem, artificial roughness on the absorber plate and jet impingement was provided. Artificial roughness acting as flow-restricting devices and jet impingement make the flow fully developed. Flow restriction devices in the form of SDASR with varying parameters and jet impingement were used in present study. Therefore, the flow inside the JISTC channel was fully developed.

Experimental Process

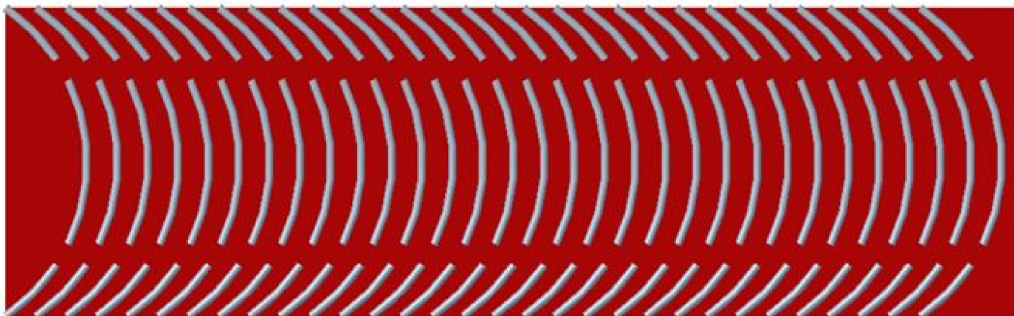
Testing was performed to record the data of SDASR-roughened plate in a rectangular JISTC channel with a jet plate for analysis of Nu_{sdr} and f_{sdr} . Each gadget was inspected precisely for its appropriate functioning in the present work. The whole intersection of the test setup was examined using a soap solution to identify any type of leakage. The apparatus, namely the U-tube manometer, voltmeter, micro-manometer, and ammeter, was used to measure the data and checked for proper functioning prior to experimentation. Nine sets of readings were taken for every roughened plate, and the mass flow rate value was varied using control valves. A digital micrometer recorded the pressure over the examination portion. An impingement jet plate was fixed among a target and base plate. The stream control valves were used to adjust the m_{sdr} of the air. For the confirmation of the steady state condition, the temperature was taken at an interval of fifteen minutes. After taking observations for the smooth absorber plate, the absorber plates with ARS in the form of SDASR of distinct parameters were fabricated for taking observations. The observations for air and absorber plate temperature at distinct locations in the channel were taken for roughened absorber plates. The recorded data for absorber plates with different

geometrical parameters at distinct m_{sdr} were used for determining Nu_{sdr} and f_{sdr} . The following experimental data were recorded for each absorber plate.

1. Pressure head variation across the orifice plate to find out the m_{sdr} .
2. Target plate temperature (T_{tp}).
3. Inlet air temperature (T_i).
4. Outlet air temperature (T_o).
5. Pressure head falls across the assessed segment (ΔP).

The absorber plates with different spacer lengths used in the examination are represented schematically in Figure 4a–d.

$S_{sdr} = 0$ mm



(a)

$S_{sdr} = 100$ mm



(b)

$S_{sdr} = 200$ mm



(c)

Figure 4. Cont.

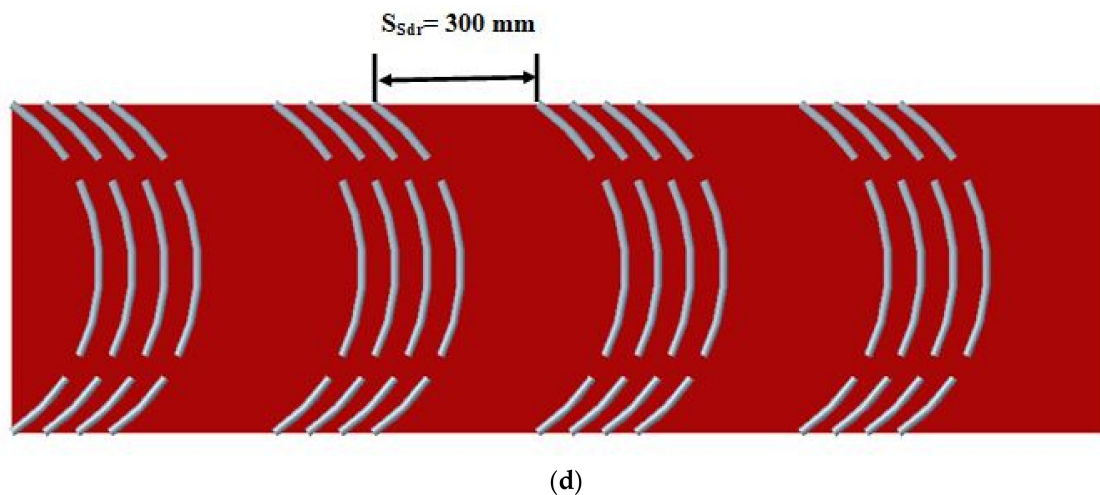


Figure 4. (a) Schematic diagram of single discrete arc-shaped ribs absorber plate (spacer length 0 mm). (b) Schematic diagram of single discrete arc-shaped ribs absorber plate (spacer length 100 mm). (c) Schematic diagram of single discrete arc-shaped ribs absorber plate (spacer length 200 mm). (d) Schematic diagram of single discrete arc-shaped ribs absorber plate (spacer length 300 mm).

4. Validation of Experimental Values

The designed experimental setup was tested for desirable outcomes consistent with previous findings. A validation test with a smooth plate was conducted before the experiment with a roughened absorber plate. The observations recorded during the validity test were used to determine Nu_{ss} and f_{ss} . The obtained results for Nu_{ss} were compared with those for Nu_{ss} calculated using the Dittus–Bolter equation [26] and the obtained results for f_{ss} were compared with those for f_{ss} determined using a modified Blasius equation [28] for rectangular passage. The Dittus–Bolter equation used to calculate Nu_{ss} and the modified Blasius equation used to calculate f_{ss} are given below:

Dittus–Bolter equation:

$$Nu_{ss} = 0.023Re^{0.8}Pr^{0.4} \quad (2)$$

where Pr is the Prandtl number.

Modified Blasius equation:

$$f_{ss} = 0.085Re^{-0.025} \quad (3)$$

After the insertion of flow restriction devices in the form of SDASR with varying parameters, the flow becomes fully developed. Therefore, after the validation test, the standard equations of fully developed flow and turbulent were used to study Nu_{sdw} and f_{sdw} . More standard correlations such as Gnielinsky and Petukhov were used to verify the results, and they showed good agreement between the experimental and the theoretical values. The Gnielinsky equation for Nu_{ss} is

$$Nu_{ss} = \frac{\frac{f_s}{8}(Re - 1000)Pr}{1 + 12.7\left(\sqrt{\frac{f_s}{8}}\right)(Pr^{2/3} - 1)} \quad (4)$$

where $f_s = [0.7904 \ln(Re) - 1.64]^{-2}$, $3000 < Re < 5 \times 10^6$.

The Petukhov equation for f_{ss} is

$$f_{ss} = [0.7904 \ln(Re) - 1.64]^{-2} \quad (5)$$

The expected and measured Nu_{ss} and f_{ss} for the smooth plate were then calculated; they are plotted in Figures 5 and 6, respectively.

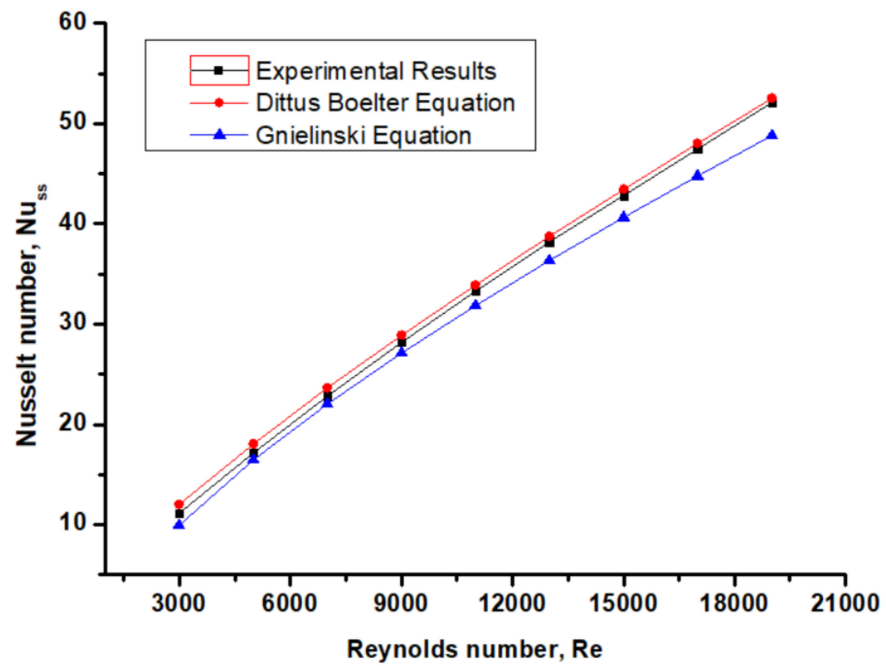


Figure 5. Comparison of experimental and predicted values for Nu_{ss} .

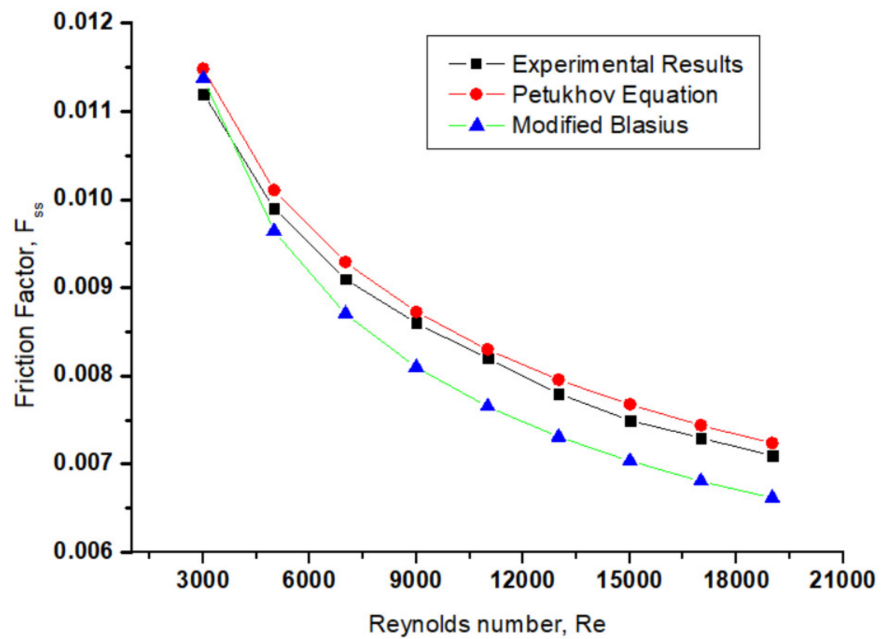


Figure 6. Comparison of experimental and predicted values for f_{ss} .

5. Data Diminution

The data collected was used to calculate h_c , Nu_{sdr} , and f_{sdr} . The essential terms for the calculation of all parameters are given below:

Temperature measured:

The weighted standard plate temperature was calculated using Equation (6) as given below:

$$T_{tp} = \frac{\sum T_i}{N} \tag{6}$$

Standard air temperature was also calculated using Equation (5) as given below:

$$T_{ma} = \frac{T_i + T_o}{2} \quad (7)$$

Mass flow rate (m_{sdr}):

The m_{sdr} was determined by the pressure reduction quantity across the standardized orifice meter by using Equation (6):

$$m_{sdr} = C_d A_0 \frac{2\rho_{ar}(\Delta p)_0^{1/2}}{1 - \beta_{oR}^4} \quad (8)$$

where $\beta_{oR} = \frac{D_o}{D_1} = 0.45$, where D_1 and D_0 are the diameter of the pipe and the diameter of the orifice meter, respectively.

Velocity of air (V_a):

$$V_a = \frac{m_{sdr}}{\rho_{ar}WH} \quad (9)$$

Hydraulic diameter:

$$D_{hy} = \frac{4 \times (W \times H)}{2 \times (W + H)} \quad (10)$$

Determination of Reynolds number:

$$Re = \frac{V_a \times D_{hy}}{\nu} \quad (11)$$

Friction factor calculation:

The f_{sdr} was calculated by data of Δp across the assessed portion length with the Darcy equation as follows:

$$f_{sdr} = \frac{2 \times \Delta p \times D_{hy}}{4 \times \rho_{ar} \times L_P \times V_a^2} \quad (12)$$

Heat transfer rate (Q_{sdr}):

$$Q_{sdr} = m_{sdr} C_p (T_o - T_i) \quad (13)$$

Heat transfer coefficient (h_c):

$$h_c = \frac{Q_{sdr}}{A_p \times (T_{ip} - T_{ma})} \quad (14)$$

Nusselt number:

$$Nu_{sdr} = \frac{h_c D_{hy}}{k_a} \quad (15)$$

6. Results and Discussion

The Nu_{sdr} and f_{sdr} characteristics of the JISTC were calculated from experimental observations obtained for SDASR with distinct roughness and flow parameters. To examine the effect of the variation of the S_{sdr} of SDASR on Nu_{sdr} and f_{sdr} characteristics, the S_{sdr} was altered from 0 mm to 300 mm in the step of 100 mm. The other parameters of SDASR, such as D_d/L_v , g_w/H_r , H_r/H , P_r/H , α_{sdr} , X_s/D_{hy} , and Y_s/D_{hy} , were kept constant.

6.1. Effect on Heat Transfer Characteristics

The experiment was performed to analyze the heat transfer improvement in the JISTC roughened with single discrete arc-shaped ribs. The D_j/D_{hy} was fixed at 0.065 because at a D_j/D_{hy} of 0.065, the diverged air jets from the perforation strike on the larger area of the absorber plate [14]. Therefore, the area of contact among air jets and absorber plates

increases. Further increases in the jet diameter ratio result in a larger contact area but also in decreases in air jet intensity, causing lower heat transfer. The plot illustrated in Figure 7 shows the impact of S_{sdr} on the Nu_{sdr} as a function of Re . The other parameters of SDASR, such as D_d/L_v , g_w/H_r , H_r/H , P_r/H , α_{sdr} , X_s/D_{hy} , and Y_s/D_{hy} , were kept constant. The present study explores the influence of parametric variations of SDASR mounted on the absorber plate on HT enhancement. The Q_{sdr} of the air was significantly increased due to the turbulence created in the flow by the ribs. The previous studies concluded that artificial roughness mounted on the absorber plate in the STC augments the HT coefficient. Artificial roughness causes increases in the friction which in turn increase the pumping power required to maintain flow in the channel. Therefore, the SDASR parameters must be optimized to keep the lowest possible f_{sdr} and maximum HT. Figure 7 shows the change in Nu_{sdr} with Re at chosen values of S_{sdr} . A rise in the HT with SDASR mounted on the absorber plate of the STC was found. The experimental findings also show that SDASR with $S_{sdr} = 0$ mm (single discrete arc-shaped ribs are mounted on the whole length of the absorber plate) had the greatest impact on HT augmentation. The findings illustrate that the S_{sdr} of the SDASR strongly affects the HT. The experiment was performed at four distinct values of S_{sdr} , from 0 mm to 300 mm with stages of 100 mm. At $S_{sdr} = 100$ mm, the flow became less turbulent and caused a drop in Nu_{sdr} . Further increases in the S_{sdr} of SDASR led to less turbulent flow. Therefore, the fluid flow became fast, and the HT of the fluid decreased, resulting in a decline in Nu_{sdr} . At $S_{sdr} = 0$ mm, the fluid was properly mixed and received the utmost heat, as shown in Figure 8. Therefore, HT was at its maximum value for the configuration in which the ribs were fixed on the entire length of the absorber plate. The impingement jets have two distinct rotating vortices that drive fluid from the colder region (internal core) towards the arc obstacle wall [39–41]. This causes the mixing of lower impingement jets with the main flow. Mixing interior stream with the main stream caused the HT among the arc ribs to suspend boundary layer formation. With rise in Re , the thickness of the boundary layer diminished due to a decrease in convective resistance, leading to enhanced Nu_{sdr} . The SDASR created a sturdy resultant stream jet behind the ribs, leading to high turbulence at the separation of impinging jets from SDASR and amalgamation with the main stream. The increase in the number of vortices added air in the STC and increased HT from the absorber plate to air.

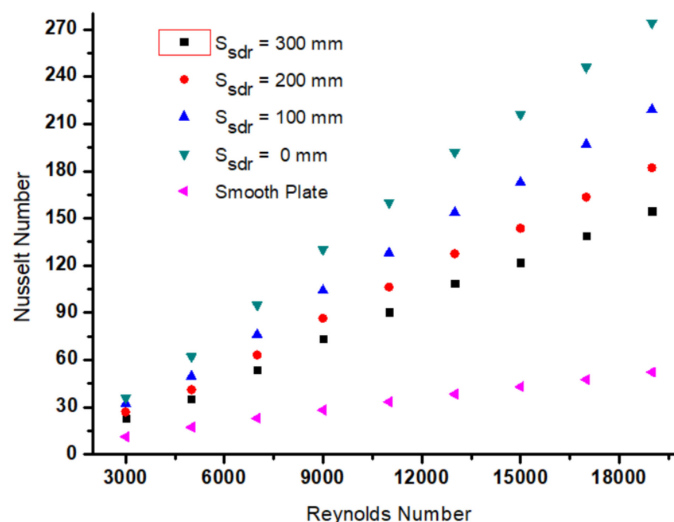


Figure 7. Variation of Nu_{sdr} with Re at different S_{sdr} .

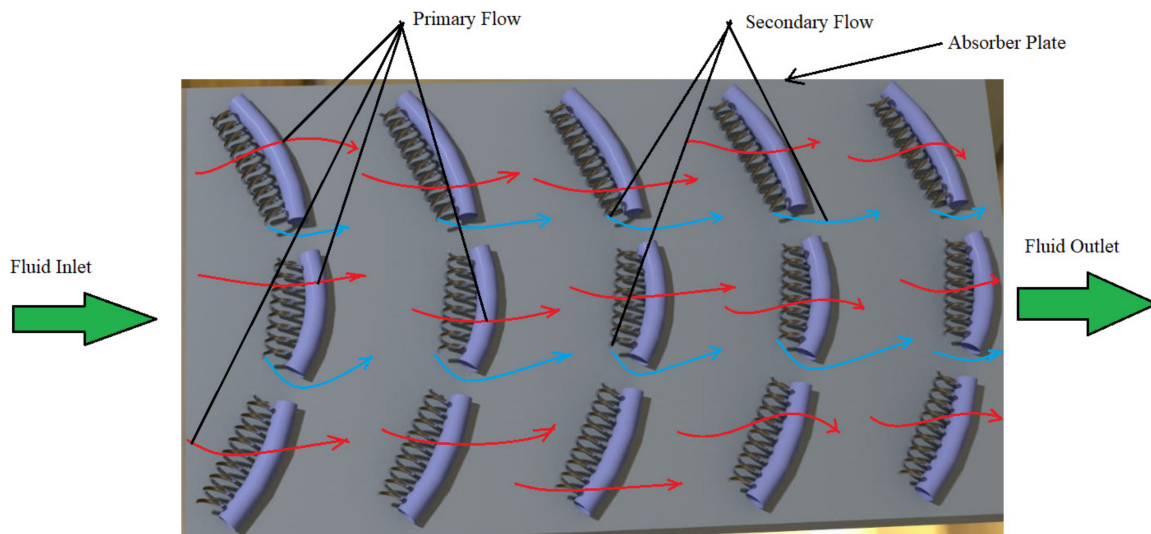


Figure 8. Flow visualization over discrete arc ribs.

6.2. Friction Factor Characteristics

Variation of f_{sdr} with Re at $S_{sdr} = 0$ mm, 100 mm, 200 mm, and 300 mm is shown in Figure 9. The S_{sdr} of the SDASR had a substantial influence on the friction factor characteristics. The fluid has to flow from obstacles after its entrance into the channel due to the presence of SDASR. The single discrete arc-shaped ribs on the absorber plate made the fluid flow turbulent and slowed down the air stream, leading to adequate HT among the air and absorber plate. Besides the enhancement in HT, the obstacles enhanced the f_{sdr} . The repetitive obstacles caused augmented HT, albeit with enhanced friction. The influence of the obstacles on the air stream decreases with an increase in the spacer length [42–45]. This is due to the discharge of the stream resulting from the presence of SDASR and the amalgamation of lower streams with the main stream.

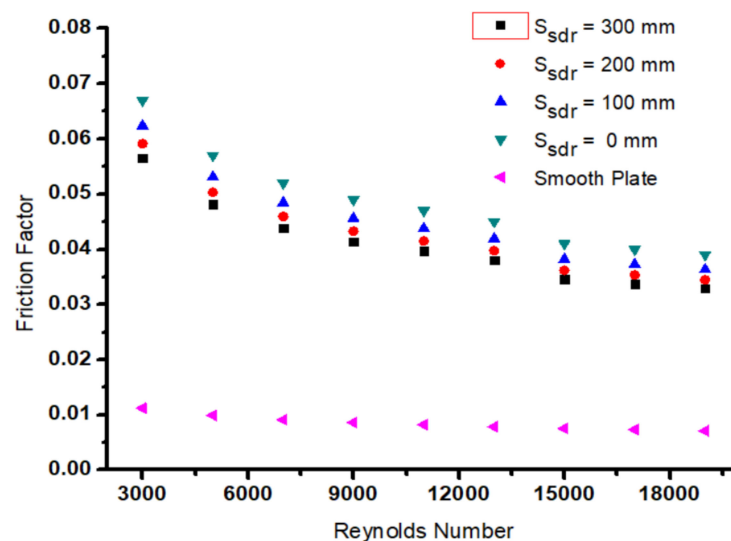


Figure 9. Variation of f_{sdr} with Re at different S_{sdr} . The artificial roughness of SDASR on the absorber plate significantly enhanced HTR but was accompanied by an augmentation in f_{sdr} losses. In the present work, the f_{sdr} characteristics of the JISTC were studied by varying the parametric values of single discrete arc-shaped ribs.

7. Thermohydraulic Performance

In the present investigation, the Nu_{sdr} and f_{sdr} of the JISTC increased with SDASR fixed on the absorber plate. As discussed in Section 6.1, the S_{sdr} of the SDASR has a significant influence on HT enhancement. The single discrete arc-shaped ribs make airflow turbulent and slow down the stream of air. This causes adequate HT among air and absorber plates. The repetitive obstacles cause augmented HT, albeit with enhanced friction. The influence of the obstacles on the air stream lowers with the increase in the spacer length. Therefore, selection of the configuration that enhances HT with the least penalty of f_{sdr} is essential. To achieve a considerable increase in heat transfer with the least penalty of f_{sdr} , the investigators [24] suggested a parameter, η_{sdr} , which is a function of Nu_{sdr} and f_{sdr} . The desired geometry must result in extreme augmentation of HT with the lowest possible friction. The η_{sdr} is determined by using following equation:

$$\eta_{sdr} = (Nu_{sdr}/Nu_{ss})/(f_{sdr}/f_{ss})^{0.33} \quad (16)$$

Figure 10 depicts different values of $\eta_{sdr} = (Nu_{sdr}/Nu_{ss})/(f_{sdr}/f_{ss})^{0.33}$ at selected S_{sdr} and Re , keeping other parameters constant. At $S_{sdr} = 0$ mm, the calculated value of η_{sdr} is 2.9, which is greater than 1. The maximum value of η_{sdr} is obtained at $S_{sdr} = 0$ mm, which suggests that the optimum performance of JISAC is at $S_{sdr} = 0$ mm.

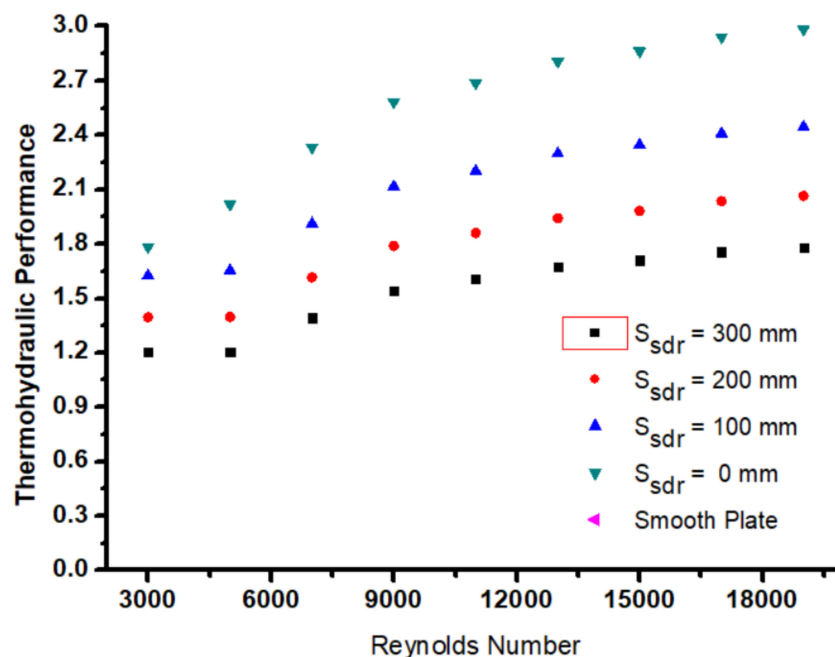


Figure 10. Variation of η_{sdr} with Re at different S_{sdr} .

8. Conclusions

From the experimental analysis of the Nu_{sdr} and f_{sdr} characteristics of the JISTC with SDASR on the absorber plate, the following conclusions can be drawn.

Attaching an SDASR on the absorber plate of a JISTC results in considerable enhancement of Nu_{sdr} . This enhancement is a strong function of jet impingement and single discrete arc-shaped ribs.

1. The single discrete arc-shaped ribs with a spacer length $S_{sdr} = 0$ mm results in increased Nu_{sdr} and f_{sdr} compared with other values of S_{sdr} .
2. The Nu_{sdr} and f_{sdr} of the JISTC with SDASR were improved by 5.25 and 5.98 times compared to the STC without SDASR.
3. The highest % increase in Nu_{sdr} and f_{sdr} of the JISTC with SDASR at $S_{sdr} = 0$ mm compared to $S_{sdr} = 300$ mm was 77% and 18%, respectively.

4. The single discrete arc-shaped ribs JSTC provided the highest η_{sdr} of 2.9 at $S_{sdr} = 0$ mm.

Author Contributions: Conceptualization, R.K., E.C., S.K., C.A.S., S.S.; methodology, R.K., E.C., S.K., S.S.; software, R.K., E.C., S.K.; validation, R.K., E.C., S.K., S.S.; formal analysis, R.K., S.K.; investigation, R.K., E.C., S.K.; resources, R.K., E.C., S.K., S.S.; data curation, R.K., E.C., S.K., S.T., P.G., B.G., C.A.S., S.S.; writing—original draft preparation, R.K., S.K.; writing—review and editing, R.K., S.K.; visualization, R.K., S.K., S.T., P.G., C.A.S.; supervision, R.K., E.C., S.K., B.G., C.A.S., S.S., C.A.S.; project administration, R.K., S.K., S.S., C.A.S.; funding acquisition, S.S.; All authors have read and agreed to the published version of the manuscript.

Funding: The authors extend their appreciation to the Deanship of Scientific Research at King Khalid University, Saudi Arabia, for funding this work through the Research Group Program under Grant No: RGP 2/26/43.

Institutional Review Board Statement: Non applicable.

Informed Consent Statement: Non applicable.

Data Availability Statement: Non applicable.

Acknowledgments: The authors extend their appreciation to the Deanship of Scientific Research at King Khalid University, Saudi Arabia, for funding this work through the Research Group Program under Grant No: RGP 2/26/43.

Conflicts of Interest: The authors declare no conflict of interest.

Nomenclature

A_p	Absorber plate surface area, mm ²
A_0	Orifice meter area, mm ²
C_p	Air specific heat, J/kg k
C_d	Coefficient of discharge
L_V	Length of single arc rib
D_d/L_v	Relative discrete distance
g_w	Discrete width
g_w/H_r	Relative discrete width
D_{hy}	Hydraulic diameter, mm
H_r	Height of rib, mm
H	Height of duct, mm
H_r/H	Relative rib height
D_j	Jet diameter, mm
D_j/D_{hy}	Jet diameter ratio
f_r	Friction factor, dimensionless
f_{sdr}	Friction factor for single discrete arc-shaped ribs, dimensionless
f_{ss}	Friction factor of smooth surface, dimensionless
h_c	Convective heat transfer coefficient, W/m ² K
k_a	Thermal conductivity, W/m K
L_p	Length of test section, mm
Nu_{sdr}	Nusselt number for single discrete arc-shaped ribs, dimensionless
Nu_{rs}	Nusselt number, dimensionless
Nu_{ss}	Smooth surface Nusselt number, dimensionless
m_{sdr}	Air mass flow rate, kg/s
Pr	Prandtl number, dimensionless
Δp	Pressure head drop across the test segment, Pa
$(\Delta p)_0$	Pressure drop across the orifice meter, Pa
Q_h	Heat transfer rate, W
Q_{sdr}	Heat transfer rate for single discrete arc ribs, W
Re	Reynolds number, dimensionless

T_{tp}	Temperature of target plate, K
T_i	Inlet air temperature, K
T_o	Outlet air temperature, K
T_{ma}	Mean air temperature, K
V_a	Velocity of air, m/s
W	Width of duct, mm
X	Streamwise variation, mm
X/D_{hy}	Streamwise variation to hydraulic diameter ratio, dimensionless
Y	Spanwise variation, mm
Y/D_{hy}	Spanwise variation to hydraulic diameter ratio, dimensionless
δy	Absolute uncertainty, dimensionless
$\delta y/y$	Relative uncertainty, dimensionless
TP	Thermal performance
HT	Heat transfer
HTR	Heat transfer rate
SAH	Solar air heater
STC	Solar thermal collector
JISTC	Jet impingement solar thermal collector
SDASR	Single discrete arc-shaped ribs
Greek Letters	
α_{sdr}	Angle of attack, degree
μ	Absolute velocity of air, Ns/m ²
ρ_{ar}	Density of air, kg/m ³
ν	Kinematic viscosity of air, m ² /s
β_R	Ratio of orifice meter to pipe diameter, dimensionless
η_h	Thermo-hydraulic performance parameter, dimensionless
η_{sdr}	Thermohydraulic performance parameter for single discrete arc-shaped ribs, dimensionless

References

- Thapa, S.; Samir, S.; Kumar, K.; Singh, S. A review study on the active methods of heat transfer enhancement in heat exchangers using electroactive and magnetic materials. *Mater. Today Proc.* **2021**, *45*, 4942–4947. [\[CrossRef\]](#)
- Thapa, S.; Samir, S.; Kumar, K. A review study on the performance of a parabolic trough receiver using twisted tape inserts. *Proc. Inst. Mech. Eng. Part E J. Process. Mech. Eng.* **2021**. [\[CrossRef\]](#)
- Dong, Z.; Liu, P.; Xiao, H.; Liu, Z.; Liu, W. A study on heat transfer enhancement for solar air heaters with ripple surface. *Renew. Energy* **2021**, *172*, 477–487. [\[CrossRef\]](#)
- Bhuvad, S.S.; Azad, R.; Lanjewar, A. Thermal performance analysis of apex-up discrete arc ribs solar air heater—an experimental study. *Renew. Energy* **2022**, *185*, 403–415. [\[CrossRef\]](#)
- Parsa, H.; Saffar-Avval, M.; Hajmohammadi, M. 3D simulation and parametric optimization of a solar air heater with a novel staggered cuboid baffles. *Int. J. Mech. Sci.* **2021**, *205*, 106607. [\[CrossRef\]](#)
- Farahani, S.D.; Shadi, M. Optimization-decision making of roughened solar air heaters with impingement jets based on 3E analysis. *Int. Commun. Heat Mass Transf.* **2021**, *129*, 105742. [\[CrossRef\]](#)
- Avargani, V.M.; Zendejboudi, S.; Rahimi, A.; Soltani, S. Comprehensive energy, exergy, enviro-exergy, and thermo-hydraulic performance assessment of a flat plate solar air heater with different obstacles. *Appl. Therm. Eng.* **2022**, *203*, 117907. [\[CrossRef\]](#)
- Saravanan, A.; Murugan, M.; Reddy, M.S.; Ranjit, P.; Elumalai, P.; Kumar, P.; Sree, S.R. Thermo-hydraulic performance of a solar air heater with staggered C-shape finned absorber plate. *Int. J. Therm. Sci.* **2021**, *168*, 107068. [\[CrossRef\]](#)
- Moshery, R.; Chai, T.Y.; Sopian, K.; Fudholi, A.; Al-Waeli, A.H. Thermal performance of jet-impingement solar air heater with transverse ribs absorber plate. *Sol. Energy* **2021**, *214*, 355–366. [\[CrossRef\]](#)
- Chauhan, R.; Singh, T.; Thakur, N.S. Investigation of the Thermal Performance of Solar Thermal Collector Provided with Impinging Air Jets. *Adv. Sci. Lett.* **2016**, *22*, 3928–3932. [\[CrossRef\]](#)
- Chaudhri, K.; Bhagoria, J.L.; Kumar, V. Transverse wedge-shaped rib roughened solar air heater (SAH)-Exergy based experimental investigation. *Renew. Energy* **2022**, *184*, 1150–1164. [\[CrossRef\]](#)
- Aboghrara, A.M.; Baharudin, B.; Alghoul, M.; Adam, N.M.; Hairuddin, A.A.; Hasan, H.A. Performance analysis of solar air heater with jet impingement on corrugated absorber plate. *Case Stud. Therm. Eng.* **2017**, *10*, 111–120. [\[CrossRef\]](#)
- Roy, S.; Patel, P. Study of heat transfer for a pair of rectangular jets impinging on an inclined surface. *Int. J. Heat Mass Transf.* **2003**, *46*, 411–425. [\[CrossRef\]](#)
- Chauhan, R.; Thakur, N. Investigation of the thermohydraulic performance of impinging jet solar air heater. *Energy* **2014**, *68*, 255–261. [\[CrossRef\]](#)
- Babic, D.; Murray, D.; Torrance, A. Mist jet cooling of grinding processes. *Int. J. Mach. Tools Manuf.* **2005**, *45*, 1171–1177. [\[CrossRef\]](#)

16. Röger, M.; Buck, R.; Müller-Steinhagen, H. Numerical and Experimental Investigation of a Multiple Air Jet Cooling System for Application in a Solar Thermal Receiver. *J. Heat Transf.* **2005**, *127*, 863–876. [[CrossRef](#)]
17. Caliskan, S.; Baskaya, S. Experimental investigation of impinging jet array heat transfer from a surface with V-shaped and convergent-divergent ribs. *Int. J. Therm. Sci.* **2012**, *59*, 234–246. [[CrossRef](#)]
18. Chang, H.; Zhang, J.; Huang, T. Experimental investigation on impingement heat transfer from rib roughened surface within arrays of the circular jet: Effect of geometric parameters. In Proceedings of the ASME 1998 International Gas Turbine and Aeroengine Congress and Exhibition, Stockholm, Sweden, 2–5 June 1998.
19. Yan, W.; Mei, S. Measurement of detailed heat transfer along rib-roughened surface under arrays of impinging elliptic jets. *Int. J. Heat Mass Transf.* **2006**, *49*, 159–170. [[CrossRef](#)]
20. Xing, Y.; Spring, S.; Weigand, B. Experimental and numerical investigation of impingement heat transfer on a flat and micro-rib roughened plate with different crossflow schemes. *Int. J. Therm. Sci.* **2011**, *50*, 1293–1307. [[CrossRef](#)]
21. Goodro, M.; Park, J.; Ligrani, P.; Fox, M.; Moon, H.-K. Effects of hole spacing on spatially-resolved jet array impingement heat transfer. *Int. J. Heat Mass Transf.* **2008**, *51*, 6243–6253. [[CrossRef](#)]
22. Huber, A.M.; Viskanta, R. Comparison of convective heat transfer to perimeter and center jets in a confined, impinging array of axisymmetric air jets. *Int. J. Heat Mass Transf.* **1994**, *37*, 3025–3030. [[CrossRef](#)]
23. Chambers, A.C.; Gillespie, D.R.H.; Ireland, P.T.; Kingston, R. Enhancement of Impingement Cooling in a High Cross Flow Channel Using Shaped Impingement Cooling Holes. *J. Turbomach.* **2009**, *132*, 021001. [[CrossRef](#)]
24. Lewis, M. Optimising the thermohydraulic performance of rough surfaces. *Int. J. Heat Mass Transf.* **1975**, *18*, 1243–1248. [[CrossRef](#)]
25. Matheswaran, M.; Arjunan, T.; Somasundaram, D. Analytical investigation of solar air heater with jet impingement using energy and exergy analysis. *Sol. Energy* **2018**, *161*, 25–37. [[CrossRef](#)]
26. Yadav, S.; Saini, R.P. Comparative study of simple and impinging jet solar air heater using CFD analysis. *AIP Conf. Proc.* **2020**, *2273*, 050043. [[CrossRef](#)]
27. Aboghrara, A.M.; Alghoul, M.A.; Baharudin, B.T.H.T.; Elbreki, A.; Ammar, A.A.; Sopian, K.; Hairuddin, A.A. Parametric Study on the Thermal Performance and Optimal Design Elements of Solar Air Heater Enhanced with Jet Impingement on a Corrugated Absorber Plate. *Int. J. Photoenergy* **2018**, *2018*, 1469385. [[CrossRef](#)]
28. Rajaseenivasan, T.; Prasanth, S.R.; Antony, M.S.; Srihar, K. Experimental investigation on the performance of an impinging jet solar air heater. *Alex. Eng. J.* **2017**, *56*, 63–69. [[CrossRef](#)]
29. Goel, A.K.; Singh, S.N. Experimental study of heat transfer characteristics of an impinging jet solar air heater with fins. *Environ. Dev. Sustain.* **2019**, *22*, 3641–3653. [[CrossRef](#)]
30. Mokashi, I.; Afzal, A.; Khan, S.A.; Abdullah, N.A.; Azami, M.H.; Jilte, R.D.; Samuel, O.D. Nusselt number analysis from a battery pack cooled by different fluids and multiple back-propagation modelling using feed-forward networks. *Int. J. Therm. Sci.* **2021**, *161*, 106738. [[CrossRef](#)]
31. Afzal, A.; Samee, A.D.M.; Razak, R.K.A.; Ramis, M.K. Steady and Transient State Analyses on Conjugate Laminar Forced Convection Heat Transfer. *Arch. Comput. Methods Eng.* **2019**, *27*, 135–170. [[CrossRef](#)]
32. Afzal, A.; Mohammed Samee, A.D.; Javad, A.; Shafvan, S.A.; Ajinas, P.V.; Ahammedul Kabeer, K.M. Heat transfer analysis of plain and dimpled tubes with different spacings. *Heat Transf.—Asian Res.* **2018**, *47*, 556–568. [[CrossRef](#)]
33. Samyalingam, L.; Aslfattahi, N.; Saidur, R.; Yahya, S.M.; Afzal, A.; Arifutzzaman, A.; Tan, K.; Kadirgama, K. Thermal and energy performance improvement of hybrid PV/T system by using olein palm oil with MXene as a new class of heat transfer fluid. *Sol. Energy Mater. Sol. Cells* **2020**, *218*, 110754. [[CrossRef](#)]
34. Soudagar, M.E.M.; Kalam, M.A.; Sajid, M.U.; Afzal, A.; Banapurmath, N.R.; Akram, N.; Mane, S.; Saleel, C.A. Thermal analyses of minichannels and use of mathematical and numerical models. *Numer. Heat Transf. Part A Appl.* **2020**, *77*, 497–537. [[CrossRef](#)]
35. Afzal, A.; Samee, A.M.; Jilte, R.; Islam, T.; Manokar, A.M.; Razak, K.A. Battery thermal management: An optimization study of parallelized conjugate numerical analysis using Cuckoo search and Artificial bee colony algorithm. *Int. J. Heat Mass Transf.* **2021**, *166*, 120798. [[CrossRef](#)]
36. Attia, M.E.H.; Driss, Z.; Kabeel, A.E.; Afzal, A.; Manokar, A.M.; Sathyamurthy, R. Phosphate bed as energy storage materials for augmentation of conventional solar still productivity. *Environ. Prog. Sustain. Energy* **2021**, *40*, e13581. [[CrossRef](#)]
37. García, D.; Prieto, J.I. A non-tubular Stirling engine heater for a micro solar power unit. *Renew. Energy* **2012**, *46*, 127–136. [[CrossRef](#)]
38. Singh, A.P.; Goel, V.; Sharma, S. Effect of artificial roughness on heat transfer and friction characteristics having multiple arc shaped roughness element on the absorber plate. *Sol. Energy* **2014**, *105*, 479–493. [[CrossRef](#)]
39. Benoudina, B.; Attia, M.E.H.; Driss, Z.; Afzal, A.; Manokar, A.M.; Sathyamurthy, R. Enhancing the solar still output using micro/nano-particles of aluminum oxide at different concentrations: An experimental study, energy, exergy and economic analysis. *Sustain. Mater. Technol.* **2021**, *29*, e00291. [[CrossRef](#)]
40. Nidhul, K.; Yadav, A.K.; Anish, S.; Arunachala, U.C. Thermo-hydraulic and exergetic performance of a cost-effective solar air heater: CFD and experimental study. *Renew. Energy* **2022**, *184*, 627–641. [[CrossRef](#)]
41. Prasad, A.R.; Attia, M.E.; Al-Kouz, W.; Afzal, A.; Athikesavan, M.M.; Sathyamurthy, R. Energy and exergy efficiency analysis of solar still incorporated with copper plate and phosphate pellets as energy storage material. *Environ. Sci. Pollut. Res.* **2021**, *28*, 48628–48636. [[CrossRef](#)]
42. Vaithilingam, S.; Muthu, V.; Athikesavan, M.M.; Afzal, A.; Sathyamurthy, R. Energy and exergy analysis of conventional acrylic solar still with and without copper fins. *Environ. Sci. Pollut. Res.* **2022**, *29*, 6194–6204. [[CrossRef](#)] [[PubMed](#)]

43. Azadani, L.N.; Gharouni, N. Multi objective optimization of cylindrical shape roughness parameters in a solar air heater. *Renew. Energy* **2021**, *179*, 1156–1168. [[CrossRef](#)]
44. Kumar, P.S.; Naveenkumar, R.; Sharifpur, M.; Issakhov, A.; Ravichandran, M.; Mohanavel, V.; Aslfattahi, N.; Afzal, A. Experimental investigations to improve the electrical efficiency of photovoltaic modules using different convection mode. *Sustain. Energy Technol. Assess.* **2021**, *48*, 101582. [[CrossRef](#)]
45. Murugan, M.; Saravanan, A.; Elumalai, P.; Kumar, P.; Saleel, C.A.; Samuel, O.D.; Setiyo, M.; Enweremadu, C.C.; Afzal, A. An overview on energy and exergy analysis of solar thermal collectors with passive performance enhancers. *Alex. Eng. J.* **2022**, *61*, 8123–8147. [[CrossRef](#)]